

Peng ZOU, Xiangming CHEN, Hao CHEN, Guanhua XU

Damage propagation and strength prediction of a single-lap interference-fit laminate structure

© Higher Education Press 2020

Abstract Experimental and finite element research was conducted on the bolted interference fit of a single-lap laminated structure to reveal the damage propagation mechanism and strength change law. A typical single-lap statically loading experiment was performed, and a finite element damage prediction model was built based on intralaminar progress damage theory. The model was programmed with a user subroutine and an interlaminar cohesive zone method. The deformation and damage propagation of the specimen were analyzed, and the failure mechanism of intralaminar and interlaminar damage during loading was discussed. The effect of secondary bending moment on load translation and damage distribution was revealed. The experimental and simulated load–displacement curves were compared to validate the developed model’s reliability, and the ultimate bearing strengths under different fit percentages were predicted. An optimal percentage was also recommended.

Keywords single-lap, interference fit, secondary bending moment, damage mechanism, bearing strength

1 Introduction

Carbon fiber-reinforced plastic (CFRP) is widely used in the aerospace industry because of its advantages, such as high specific strength, high specific stiffness, and good fatigue resistance. Many mechanical joints still exist in structures due to limitations in the requirements of

composite forming and maintenance. Among these joints, the bolt joint has become the main connection form of aircraft bearing structures because of its strong bearing capacity, easy disassembly, and other advantages. In practical applications, the stress concentration on the hole wall is a key contributor to structural failure. Relevant research has shown that composite joint failure accounts for 60%–80% of the total structural failure and is a problem that restricts composite application [1]. Therefore, the reduction of stress concentration and improvement of bearing capacity are crucial in ensuring the safety of connection structures.

As a new type of joint, the composite interference-fit joint is developed from metal interference ones. This joint has great potential in reducing the stress concentration around the hole because of the close contact between the pin and hole and has thus attracted considerable research attention [1–9]. However, the interference interface is prone to wear and delamination because of the special anisotropy and low interlaminar strength of the composite, and this vulnerability challenges the composite’s bearing reliability. Therefore, studying the damage mechanism and bearing capacity during installation and loading is essential, and the relationship between interference and strength must be clarified.

Relevant scholars [1–9] have conducted extensive, meaningful research. Reference [2] investigated the interface damage behavior of titanium alloy/CFRP and titanium alloy/titanium alloy under different interference during the installation of a CFRP/titanium alloy interference-fit structure. The study revealed that the wear particles produced by CFRP damage have a certain lubricating effect on the wall. Reference [3] studied the delamination of the hole wall during installation. A critical delamination force model based on type I delamination was established, and the critical delamination interference was predicted. In Ref. [4], various damage modes were considered, and hole wall quality under different interference was systematically analyzed. In Ref. [5], the drilling accuracy and bolt modification of interference joints were studied, and the

Received January 2, 2020; accepted March 26, 2020

Peng ZOU (✉), Xiangming CHEN, Hao CHEN
Full Scale Aircraft Structural Static/Fatigue Laboratory, AVIC Aircraft Strength Research Institute of China, Xi’an 710065, China
E-mail: zoupeng_0625@126.com

Guanhua XU
School of Mechanical Engineering, Northwestern Polytechnical University, Xi’an 710072, China

reliability of the developed scheme was verified through experiments. This work showed that current research on the installation damage of interference joints is thorough. On this basis, a new type of interference connection fastener was proposed to reduce the possibility of damage during installation. In addition, many useful attempts have been made to study static loading and fatigue properties. Liu et al. [6] comprehensively analyzed the influence of interference and bolt preload on the bearing capacity of a structure. Zou et al. [7] analyzed and predicted the loading failure mechanism and bearing strength of a double-lap structure. References [8,9] studied the fatigue performance of interference connection structures and found that reasonable interference can effectively improve the fatigue life of structures.

Current research on the static loading process focuses on the influence of interference percentage and preload, whereas research on the effect of secondary moment characteristics of single-lap structures remains lacking. Therefore, the present work focused on the experimental and finite element study of CFRP single-lap structures affected by secondary bending moment and interference.

The damage propagation mechanism and bearing strength under different interference were analyzed and predicted. The secondary bending moment effect was revealed to provide support for structural design.

2 Experimental study

2.1 Specimen preparation

As shown in Fig. 1, the composite single-lap interference joint structure is mainly composed of two CFRP plates and one Ti alloy bolt. This structure is common in aircraft. Its failure mechanism is affected by the load form and related to the secondary bending moment. The detailed dimensions of the test pieces in accordance with the ASTM D5961/D5961M standard are also shown in Fig. 1. The composite laying sequence is $[0/\pm 45/90]_2S$, and the nominal thickness of a single layer is 0.25 mm. The material properties are shown in Table 1. The titanium alloy bolt material is Ti-6Al-4V, and its material properties are shown in Table 2.

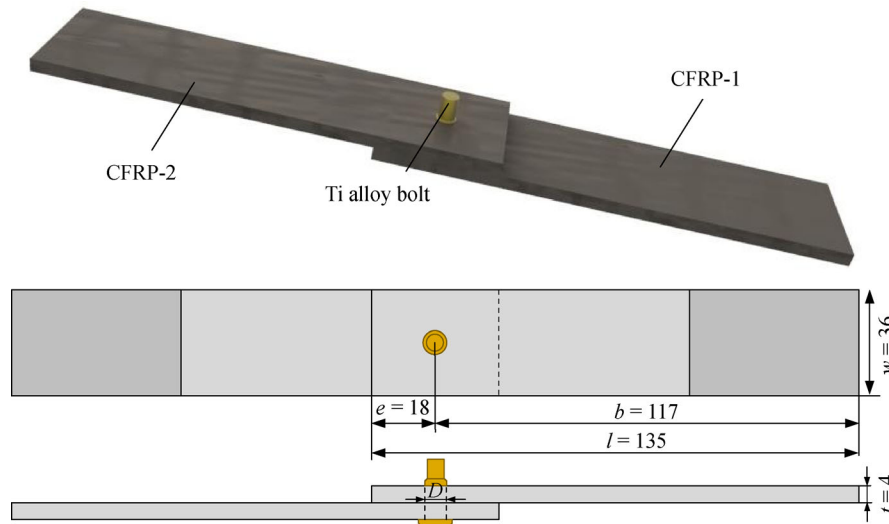


Fig. 1 Configuration and dimension of the specimen. Unit: mm.

Table 1 Properties of T700/BA9916

Property	Value	Property	Value
Longitudinal modulus, E_1 /GPa	114	Longitudinal tensile strength, X_t /MPa	2688
Transverse modulus, E_2 /GPa	8.61	Longitudinal compression strength, X_c /MPa	1458
Transverse modulus, E_3 /GPa	8.61	Transverse tensile strength, Y_t /MPa	69.5
Shear modulus, G_{12} /GPa	4.16	Transverse tensile strength, Z_t /MPa	55.5
Shear modulus, G_{13} /GPa	4.16	Transverse compression strength, Y_c /MPa	236
Shear modulus, G_{23} /GPa	3	Transverse compression strength, Z_c /MPa	175
Poisson's ratio, ν_{12}	0.3	Shear strength, S_{12} /MPa	136
Poisson's ratio, ν_{13}	0.3	Shear strength, S_{13} /MPa	136
Poisson's ratio, ν_{23}	0.45	Shear strength, S_{23} /MPa	95.6

Table 2 Properties of the bolt

Material	Young's modulus	Poisson's ratio	Tensile strength	Yield strength
Ti-6Al-4V	112 GPa	0.29	931 MPa	862 MPa

2.2 Experimental process

The experiment was completed on an Instron universal testing machine (Fig. 2). Before loading, the high lock bolt was pressed onto the test piece through the machine for pre-connection. The interference percentages were 0%, 0.4%, 0.8%, and 1.2%. The interference quantity is defined in Eq. (1). Each group of interference was tested three times in the experiment, and the loading speed was set to 2 mm/min.

$$I\% = \frac{D-d}{d} \times 100\%, \quad (1)$$

where D is the diameter of the high lock bolt, d is the diameter of the hole, and $I\%$ is the theoretical or relative interference.

3 Finite element model

Composite damage includes intralaminar and interlaminar damage between layers (delamination). Delamination is a common damage form that usually interacts with and promotes the intralaminar damage within a layer (fiber or matrix damage). Structural stiffness decreases with delamination propagation, and this decrease aggravates the occurrence of intralaminar damage. Intralaminar damage in turn causes high lateral shear load, additional

stiffness, and strength degradation, all of which aggravate the propagation of delamination [10]. Therefore, intralaminar and interlaminar damages are concomitant and must be considered simultaneously during modeling.

3.1 Model building

The finite element model was implemented in ABAQUS 6.14 with a standard solver. Figure 3 shows the meshed single lap specimen model with three parts, namely, two composite plates and one bolt. The bolt was simulated with 2412 C3D8R and 792 C3D6 elements. The plate was modeled with 83712 C3D8R elements and simulated with a layer of solid elements for each individual layer. Internal cohesive element layers with 78480 COH3D3 elements were embedded on the plate. The meshes in the contact area were more refined than those in the other areas to obtain balance between computing time and result accuracy. Twelve elements were distributed along the radial direction in the refined area around the hole. The length of each element was approximately 0.253 mm. Ninety-six elements were distributed along the circumference, and the length of each element along the hole circumference was 0.194 mm. The aspect ratio of the elements around the hole was 1.3 to ensure the accuracy of the calculation results. A mesh convergence test was conducted and showed that the results are independent of the element size. Three contact pairs existed between the

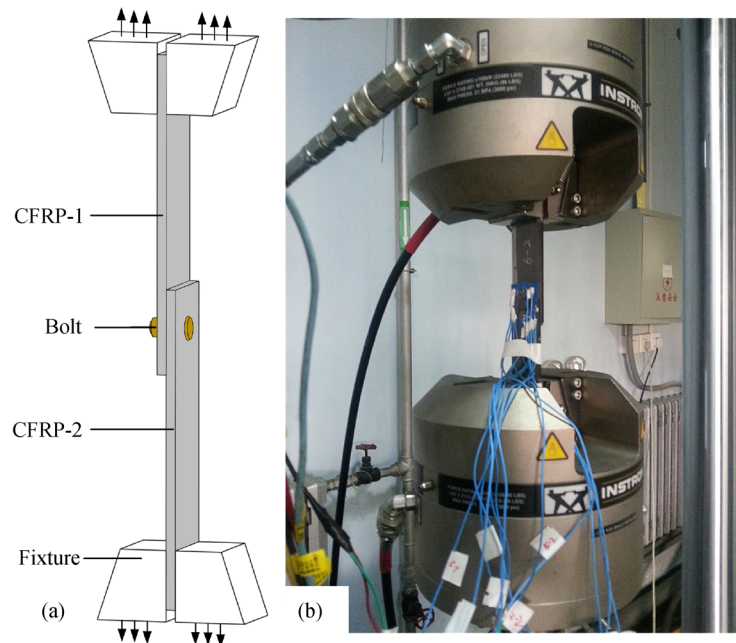


Fig. 2 Single-lap interference-fit laminate structure experimental loading procedure: (a) Specimen configuration, and (b) experimental facility and procedure.

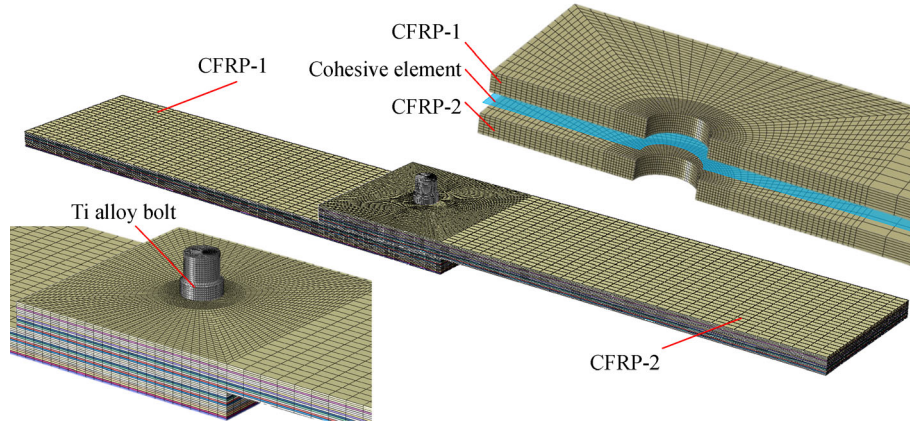


Fig. 3 Single-lap interference-fit laminate structure finite element model.

bolt shank and composite hole, that is, the bolt end and composite material and two composite plates. The contact property was set as limited slipping, and the contact relationship was set as normal hard contact and tangent valve contact. The tangent friction coefficient was based on related literature [1,6], and the coefficients were separately set as 0.1, 0.4, and 0.1 between the bolt and hole, upper and lower composite plates, and bolt end and composite plate, respectively. Interference fit modeling was realized by designing corresponding diameters of the bolt and hole without using the interference fit function in the ABAQUS software because the mechanism of the interference fit function in this software is realized by removing the master and slave nodes, which differ from the real fit condition. Two main steps were implemented to realize interference fit and loading with different boundary conditions and loads. In the first step, a displacement load parallel to the bolt axis was applied to install the bolt and form the interference. In the second step, one end of a plate was restrained and the other was applied with a displacement load. The strain-rate sensitivity was disregarded in the simulation because of the low and constant loading speed [11].

3.2 Damage prediction model

The composite damage mechanism was simulated with the intralaminar progressive damage model and the interlaminar delamination model [11–13]. The metal bolt was simulated as an elastic one with the elastic modulus shown in Table 2.

3.2.1 Intralaminar progressive damage model

The failure of the fiber and matrix in three directions and the shear failure of the fiber matrix interface should be considered because of the 3D stress status in the loading process. In addition, the corresponding properties degrade when damage occurs. Therefore, the determination of

failure and attribute degradation criteria is essential in model building. The Hashin failure criterion is widely accepted because of its full consideration of various failure modes. Moreover, the nonlinear shear stress–strain behavior is an important factor to be considered [14]. Therefore, modified Hashin failure criteria were used in this study, as shown below:

1) Fiber failure

$$e_{ft}^2 = \left(\frac{\sigma_1}{X_t} \right)^2, \sigma_1 \geq 0, \quad (2)$$

$$e_{fc}^2 = \left(\frac{\sigma_1}{X_c} \right)^2, \sigma_1 \leq 0, \quad (3)$$

where e_{ft} and e_{fc} are the indexes of fiber tensile and compression failure, respectively, σ_1 is the longitudinal tensile and compression stress, and X_t and X_c are the corresponding tensile and compression strength, respectively.

2) Fiber-matrix shear out failure

$$e_{fs}^2 = \left(\frac{\sigma_1}{X_c} \right)^2 + \frac{2\tau_{12}^2/G_{12}^0 + 3\alpha\tau_{12}^4}{2S_{12}^2/G_{12}^0 + 3\alpha S_{12}^4} + \frac{2\tau_{13}^2/G_{13}^0 + 3\alpha\tau_{13}^4}{2S_{13}^2/G_{13}^0 + 3\alpha S_{13}^4}, \sigma_1 \leq 0, \quad (4)$$

where e_{fs} is the index of fiber-matrix shear-out failure, σ_1 is the longitudinal compression stress, τ_{12} and τ_{13} are the shear stresses, G_{12}^0 and G_{13}^0 are the shear moduli, S_{12} and S_{13} are the shear strengths, and α is a material parameter.

3) Matrix tensile failure

$$e_{mt}^2 = \left(\frac{\sigma_2}{Y_t} \right)^2 + \frac{2\tau_{12}^2/G_{12}^0 + 3\alpha\tau_{12}^4}{2S_{12}^2/G_{12}^0 + 3\alpha S_{12}^4} + \frac{2\tau_{23}^2/G_{23}^0 + 3\alpha\tau_{23}^4}{2S_{23}^2/G_{23}^0 + 3\alpha S_{23}^4}, \sigma_2 \geq 0, \quad (5)$$

$$e_{mt3}^2 = \left(\frac{\sigma_3}{Z_t}\right)^2 + \frac{2\tau_{13}^2/G_{13}^0 + 3a\tau_{13}^4}{2S_{13}^2/G_{13}^0 + 3aS_{13}^4} + \frac{2\tau_{23}^2/G_{23}^0 + 3a\tau_{23}^4}{2S_{23}^2/G_{23}^0 + 3aS_{23}^4}, \sigma_3 \geq 0, \quad (6)$$

where e_{mt2} and e_{mt3} are the matrix tensile failure indexes in in-plane and out-of-plane directions, respectively, σ_2 and σ_3 are the transverse tensile stresses, and Y_t and Z_t are the corresponding tensile strengths.

4) Matrix compression failure

$$e_{mc2}^2 = \left(\frac{\sigma_2}{Y_c}\right)^2 + \frac{2\tau_{12}^2/G_{12}^0 + 3a\tau_{12}^4}{2S_{12}^2/G_{12}^0 + 3aS_{12}^4} + \frac{2\tau_{23}^2/G_{23}^0 + 3a\tau_{23}^4}{2S_{23}^2/G_{23}^0 + 3aS_{23}^4}, \sigma_2 \leq 0, \quad (7)$$

$$e_{mc3}^2 = \left(\frac{\sigma_3}{Z_c}\right)^2 + \frac{2\tau_{13}^2/G_{13}^0 + 3a\tau_{13}^4}{2S_{13}^2/G_{13}^0 + 3aS_{13}^4} + \frac{2\tau_{23}^2/G_{23}^0 + 3a\tau_{23}^4}{2S_{23}^2/G_{23}^0 + 3aS_{23}^4}, \sigma_3 \leq 0, \quad (8)$$

where e_{mc2} and e_{mc3} are the corresponding matrix compression failure indexes in-plane and out-of-plane directions, respectively, Y_c is the transverse compressive strength, and Z_c is the out-of-plane compressive strength.

When one of the Hashin damage criteria is satisfied, the value obtained from the corresponding damage evolution law is used to change or degrade the corresponding stiffness value [11]. The material is damaged and stiffness begins to degrade as the load increases, eventually leading to a decrease in bearing capacity. In this study, the degradation criterion proposed by Olmedo et al. [15] was adopted, as shown in Table 3.

The intralaminar progressive damage model was implemented in ABAQUS with the subroutine USDFLD. Seven field variables (FVs) were built to control the material properties, which are failure indices of fiber tension/compression, fiber–matrix shear, and matrix failure in in-plane and out-of-plane directions. The flowchart of the simulation procedure is shown in Fig. 4. In the beginning of the simulation, the FVs and corresponding

solution-dependent state variables (SDVs) were set to zero, and the material properties were unchanged. Iterations were performed with increasing load until convergence was reached. The stress, strain, failure indices, and shear damage parameters were calculated once the model reached a balanced state, and the failure indices were stored as SDVs. The corresponding FVs were changed to 1.0 when the SDVs exceeded 1.0 until the analysis ended. As the SDVs increased from 0 to 1.0, the material properties were automatically reduced in accordance with the degradation rules. After several iterations and load increments, convergence became difficult to achieve, and the model finally failed [4].

3.2.2 Interlaminar delamination model

The cohesive element method based on fracture mechanics was used to simulate the delamination damage [16]. The simulation process included damage initiation and propagation. The bilinear traction separation constitutive model that characterizes delamination is shown in Fig. 5.

The normal and tangential uncoupled constitutive behaviors of the cohesive interface layer are expressed as follows:

$$\begin{Bmatrix} t_n \\ t_s \\ t_t \end{Bmatrix} = \begin{bmatrix} K_n & 0 & 0 \\ 0 & K_s & 0 \\ 0 & 0 & K_t \end{bmatrix} \begin{Bmatrix} \varepsilon_n \\ \varepsilon_s \\ \varepsilon_t \end{Bmatrix}, \quad (9)$$

where t_n represents the normal (n) nominal traction force, t_s and t_t are two tangential nominal traction forces in separation (s) and traction (t) directions, ε_n , ε_s , and ε_t represent the corresponding nominal strain values, and K_n , K_s , and K_t are the interface stiffness values.

K_i ($i = n, s, t$) is expressed as

$$K_i = \begin{cases} K_i^0 & \varepsilon_i \leq \varepsilon_i^0, \\ (1-d_i)K_i^0 & \varepsilon_i^0 \leq \varepsilon_i \leq \varepsilon_i^f, \\ 0 & \varepsilon_i \geq \varepsilon_i^f, \end{cases} \quad i = n, s, t, \quad (10)$$

where K_i^0 is the initial interface stiffness, ε_i^0 and ε_i^f are the corresponding nominal strain values for delamination initiation and completion in the single mode, respectively, and d_i is the damage variable that controls delamination

Table 3 Property degradation rules of T700/BA9916

Failure mode	E_1	E_2	E_3	G_{12}	G_{13}	G_{23}	ν_{12}	ν_{13}	ν_{23}
Fiber tension failure ($\sigma_1 \geq 0$)	0.14	0.4	0.4	0.25	0.25	0.2	0	0	0
Fiber compression failure ($\sigma_1 \leq 0$)	0.14	0.4	0.4	0.25	0.25	0.2	0	0	0
Fiber–matrix shear out failure ($\sigma_1 \leq 0$)	–	–	–	0.25	0.25	–	0	0	–
In-plane matrix tension failure ($\sigma_2 \geq 0$)	–	0.4	0.4	–	–	0.2	0	0	0
In-plane matrix compression failure ($\sigma_2 \leq 0$)	–	0.4	0.4	–	–	0.2	0	0	0
Out-of-plane matrix tension failure ($\sigma_3 \geq 0$)	–	0.4	0.4	–	–	0.2	0	0	0
Out-of-plane matrix compression failure ($\sigma_3 \leq 0$)	–	0.4	0.4	–	–	0.2	0	0	0

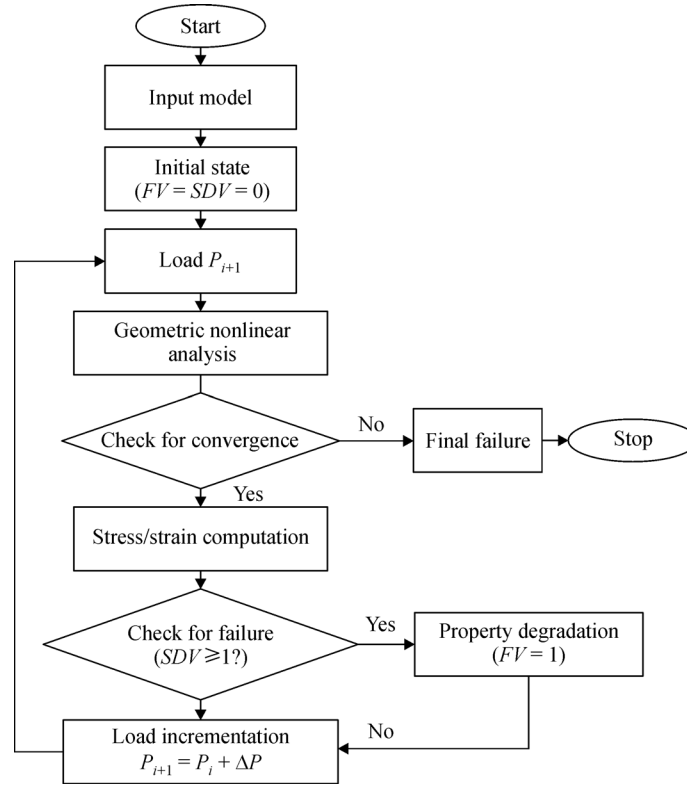


Fig. 4 Flowchart of the simulation procedure.

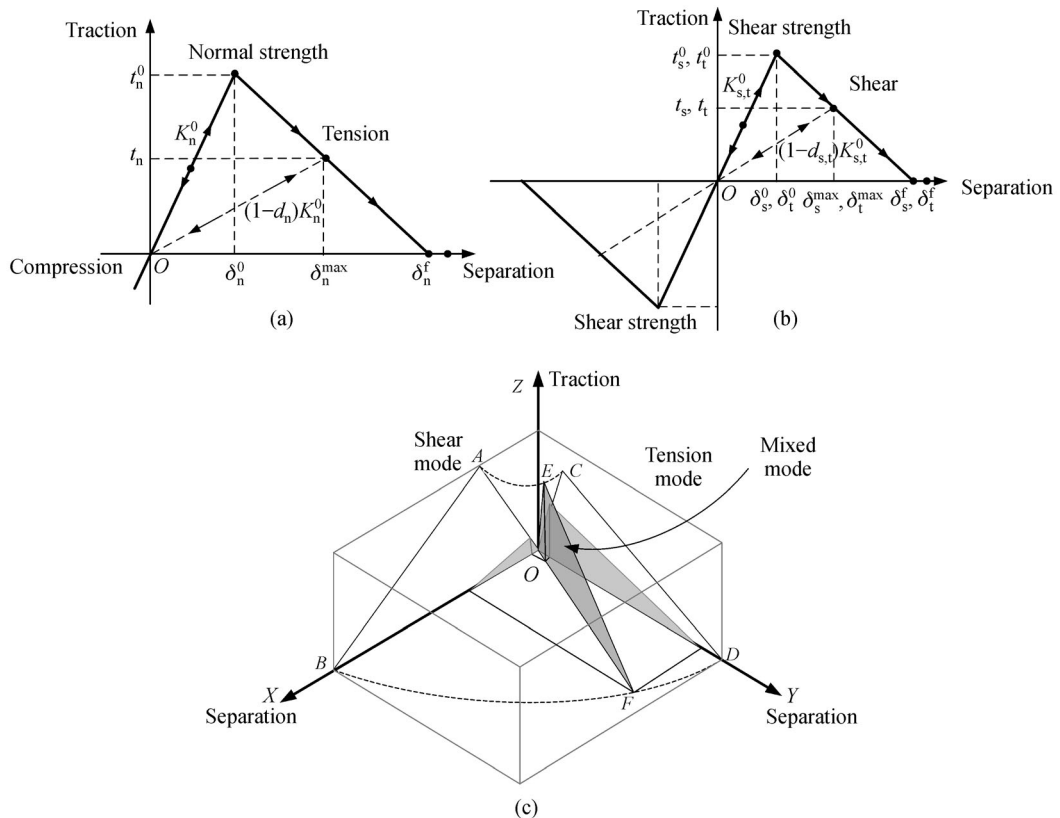


Fig. 5 Cohesive double linear constitutive model [3]: (a) Normal behavior, (b) shear behavior, and (c) mixed mode.

propagation. After delamination initiation, the interface layer delamination behavior is controlled by the delamination softening law. The law of linear softening based on energy can be expressed as

$$d_i = \frac{\varepsilon_i^f (\varepsilon_i^{\max} - \varepsilon_i^0)}{\varepsilon_i^{\max} (\varepsilon_i^f - \varepsilon_i^0)}, \quad (11)$$

where ε_i^{\max} is the maximum effective displacement during loading.

In the loading process, delamination is the interactive result of normal and tangential forces. Therefore, the secondary nominal stress criterion is used to predict the initiation of mixed mode delamination. Delamination begins to occur when the traction stress rate meets the following criteria:

$$\left\{ \frac{\langle t_n \rangle}{t_n^0} \right\}^2 + \left\{ \frac{t_s}{t_s^0} \right\}^2 + \left\{ \frac{t_t}{t_t^0} \right\}^2 = 1, \quad (12)$$

where the $\langle \rangle$ symbol is a Macaulay bracket indicating that the compressive load does not cause delamination.

Once delamination is initiated, it begins to expand between layers. The interface stiffness degenerates in accordance with the softening law. Delamination displacement further increases with the degradation of stiffness. The delamination fracture energy is consumed until visible delamination occurs. In this study, the energy law [17,18] was used to define mixed-mode delamination failure, as shown in Eq. (13):

$$\left[\frac{G_n}{G_n^C} \right]^\beta + \left[\frac{G_s}{G_s^C} \right]^\beta + \left[\frac{G_t}{G_t^C} \right]^\beta = 1, \quad (13)$$

where G_n , G_s , and G_t are instantaneous fracture energy in three directions, and G_n^C , G_s^C , and G_t^C are the critical fracture energy of normal and two tangential stratifications under the single mode. β is an empirical parameter that characterizes the coupling degree of three stratified modes. A value of 1 is used here for β [18–23].

Material properties of cohesive element used in this research are listed below, part of which are experimentally obtained, and the parameters are verified in Ref. [3]:

Critical energy release rate in mode I delamination: $G_{IC} = 0.28 \text{ mJ/mm}^2$;

Critical energy release rate in mode II or III delamination: $G_{IIC} = G_{IIIC} = 0.82 \text{ mJ/mm}^2$;

Interface strength: $t_n^0 = t_s^0 = t_t^0 = 60 \text{ MPa}$;

Initial interface stiffness: $K = 0.8 \times 10^6 \text{ N/mm}^3$;

Viscosity coefficient: $\mu = 10^{-4}$.

4 Result discussion

Different from the tensile load for a double-lap structure, the tensile load for a single-lap structure acts on the middle surface of two plates [24]. Additional bending moment and out-of-plane deformation occur at the connection zone of the structure due to eccentric load, and this occurrence is called the secondary bending moment [25]. The secondary bending moment changes the local stress and strain field and affects the bearing capacity of the joint. Therefore, the mechanical behavior of single-lap structures is more complex than that of double-lap structures.

4.1 Deformation analysis

Figure 6 shows the deformation diagram obtained from the finite element simulation and experiment. Several typical characteristics of the single-lap joint, such as secondary bending moment, bolt torsion, and contact surface separation of the two plates, can be seen in Fig. 6. These phenomena are mainly caused by the eccentric load and would eventually change the stress distribution, resulting in an inconsistent damage distribution in the thickness direction. Such damage aggravates the bearing of local layers and thus causes adverse effects on the structure. However, bolt torsion and plate separation can be delayed or restrained by applying a certain amount of interference and preload, and the bearing capacity can be improved.

4.2 Experimental result analysis

The section diagram of the single-lap specimen is shown in

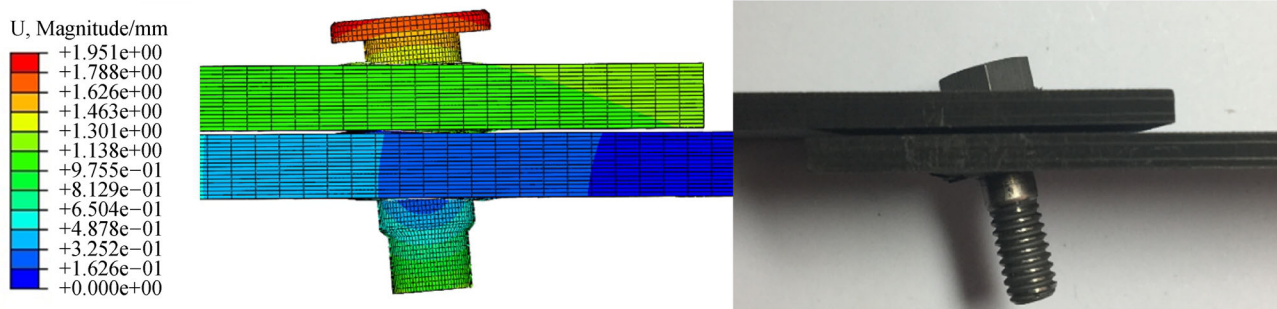


Fig. 6 Deformation cloud of the single-lap interference-fit structure.

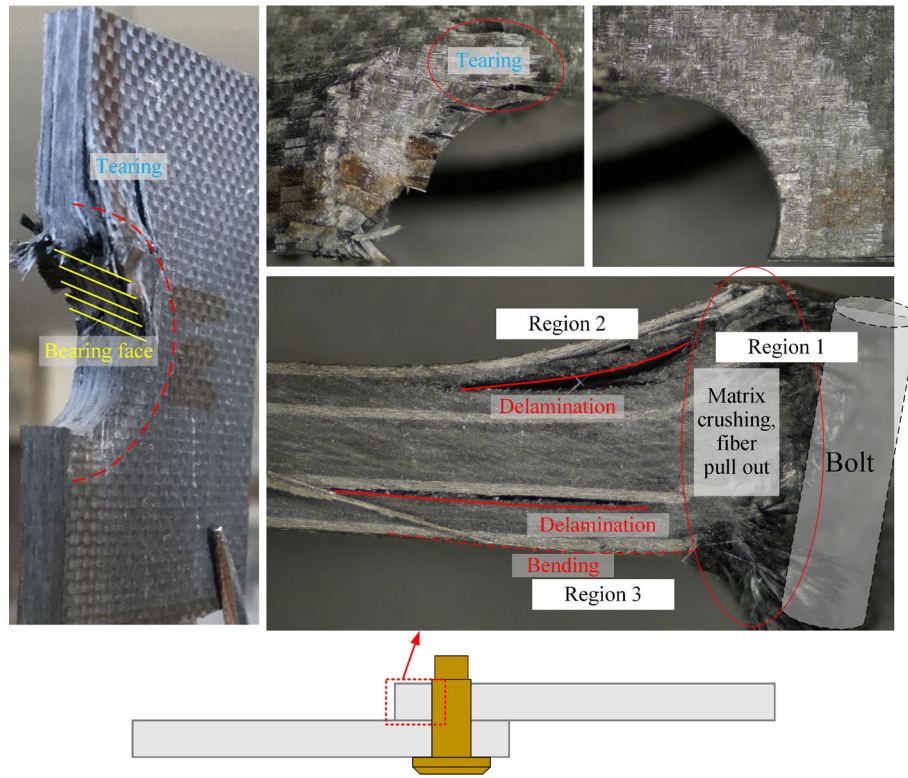


Fig. 7 Damages on the middle section of the specimen.

Fig. 7. The damage can be divided into three regions: Region 1: The damage region of pin-hole contact surfaces; Region 2: The damage region of composite external layers; and Region 3: The damage region of two plates contacting layers. Damages initially occurred in Region 1, which is characterized by contact surface collapse, including matrix collapse, micro buckling caused by fiber precipitation or compression failure, and delamination caused by these failures. The crushing damage in this area was noticeable near the surface of the specimen, and the deformation of the bolt shank further increased the load on the hole surface. However, the impact of extrusion damage on the load–displacement curve was minimal and not the main cause of the extrusion failure for the entire specimen. When the damage accumulated and reached a certain saturation state, Regions 2 and 3 expanded along the loading direction. Delamination occurred easily in these two regions. The delamination in Region 2 was mainly caused by axial force from bolt inclination, load increase, and tearing of the hole wall. The delamination mode was mainly open type. Meanwhile, the delamination in Region 3 was mainly caused by the extrusion effect of the bolt on the test piece, which resulted in slide delamination. In addition, delamination deflection occurred on the lower surface because of the bolt extrusion and lower layer plate contact support.

4.3 Finite element result analysis

4.3.1 Intralaminar damage

The damage distribution was uneven along the hole thickness direction because of the influence of the secondary bending moment. The intralaminar damage around the hole when the tensile displacement is 1 mm is shown in Fig. 8. The main damage types were in-plane and out-of-plane matrix compression failure and fiber–matrix shear failure. Given that the bolt rotated obliquely during the loading process, damage initially occurred near the upper and lower surfaces then extended along radial and axial directions, showing apparent inconsistency. The distribution of damage along the thickness direction revealed that the load-bearing behavior was localized. Only a small part of the layers bore most of the load.

4.3.2 Interlaminar delamination

Figure 9 shows the deletion of cohesive element layers, which represents delamination. The non-uniform distribution of delamination in the thickness direction was highly apparent due to the existence of the secondary bending moment. During loading, the load was applied on the left side of the upper plate, and the right side of the lower plate

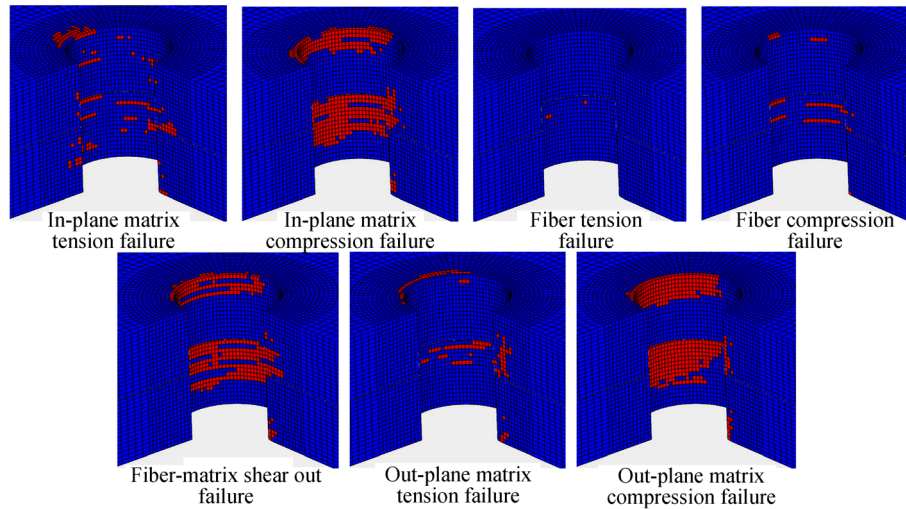


Fig. 8 Intralaminar damage around the hole.

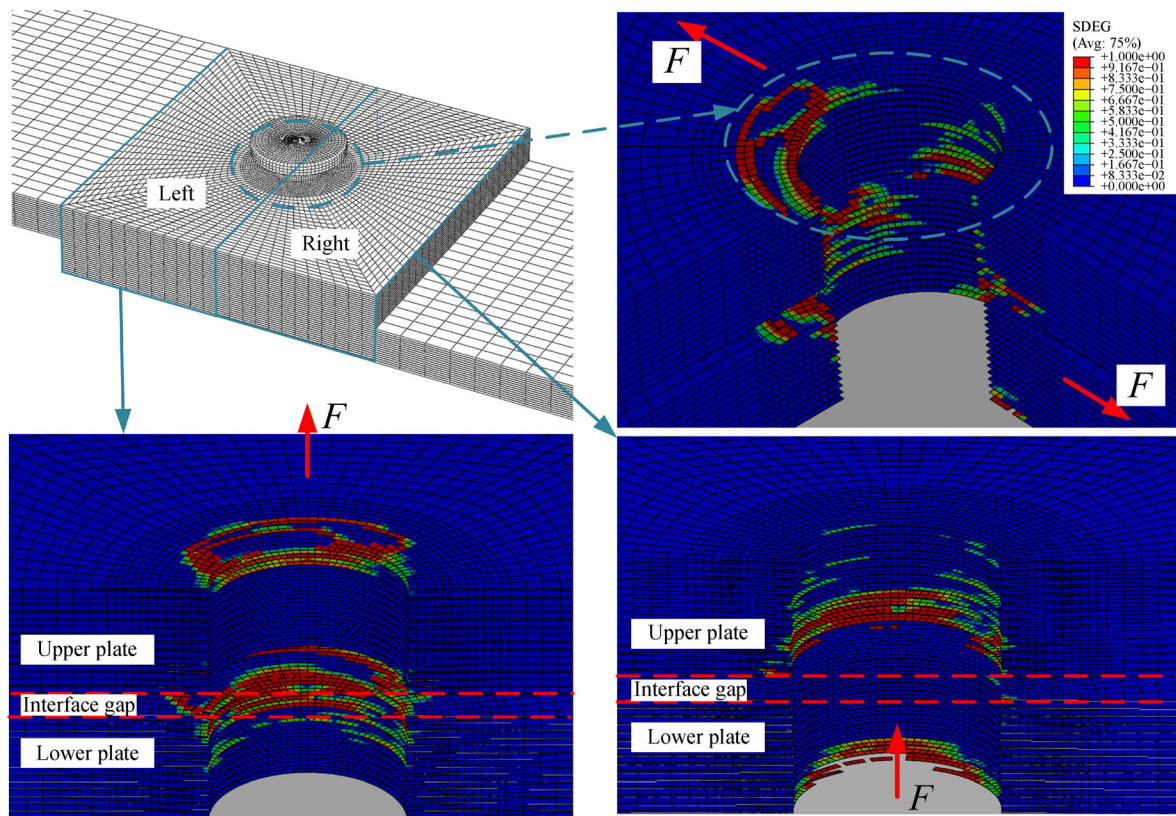


Fig. 9 Delamination around the hole.

was fixed. For the upper plate, the delamination damage in the upper left and lower right corners around the hole was noticeable. The same delamination distribution occurred on the lower plate (i.e., mainly concentrated in the upper left and lower right corners). In addition, a large interlayer gap can be seen in the figure, indicating that the two

composite plates experienced relative sliding along the thickness direction; this situation should be effectively restricted by the preload. Reference [24] showed that the fracture energy of delamination propagation is not a material constant in mode II-dominated delamination, which is linearly related to the stress in the thickness

direction. With the increase in compression load, the fracture energy, that is, the ability to restrain delamination propagation, also increases. Therefore, delamination can be effectively restrained by increasing the clamping force. In addition, the friction between composite plates also increases with the increase in the binding force in the thickness direction, which further leads to an increase in joint strength.

With increasing load, two changes occurred in the structure, namely, bolt leaned around the central axis and joint surface separation of the two plates, as shown in Fig. 10. Then, delamination occurred on the contact surfaces of the two plates and gradually extended along the axial and radial directions. This occurrence is mainly due to the fact that during the loading process, the main extrusion region was located here, and the possibility of type II delamination was further increased. With the increase in bolt rotation angle, the separation degree of the joint surface became increasingly serious. Laminated plates that had already been delaminated were flexed because of the compression of the bolt and the action of adjacent layers. Delamination protruded to the outside of the plate, and the joint surfaces separated due to the protruding flexure. All these phenomenon can be seen in Fig. 10.

4.4 Mechanism of secondary bending moment

Figure 10 shows that the delamination damage of the two plates was symmetrically distributed with respect to the contact surface, and the delamination was relatively serious in the contact area. The reasons can be found in Fig. 11. According to the load condition, the contact surface of the pin and hole can be divided into two areas:

Active and passive load-bearing surfaces. The active load-bearing surface is close to free edge of the composite plate, which becomes the main load-bearing area during the loading process. The other side is defined as the passive load-bearing surface, which also bears load mainly because of the secondary bending moment.

In the initial stage in this study, the bolt had not undergone large rotation, and the surfaces in R_1 , R_2 , R_3 , and R_4 around the hole were in contact with the bolt shank. For bearing surfaces R_1 and R_2 , the load increased along the radial direction, and for surfaces R_3 and R_4 , the extrusion effect was gradually reduced because of the interference. When the load increased to a certain extent, the bolt rotated. At this time, the contact area between bolt shank and hole wall was reduced. However, the squeezed displacement load of the active load-bearing surface along the loading direction increased because of the load influence, and the passive load-bearing surface was also squeezed by the bolt rod accordingly. Figure 11(b) shows that although the screw shank extrusion displacement caused by bolt rotation was far away from the contact surface of the two plates, the external load also stretched the two plates to move to both sides. Hence, the extrusion degree of the active load-bearing surface was greater than that of the passive load-bearing surface, which explains why the damage of the contact surface area was more serious than that of the other two sides. In addition to the movement along the stretching direction, the contact surfaces of the two plates also gradually separated.

When no lateral restraint force was present, the stress was concentrated in the squeezed area, and the upper and lower surface areas of the composite plates were prone to delamination. However, when a certain restraint force

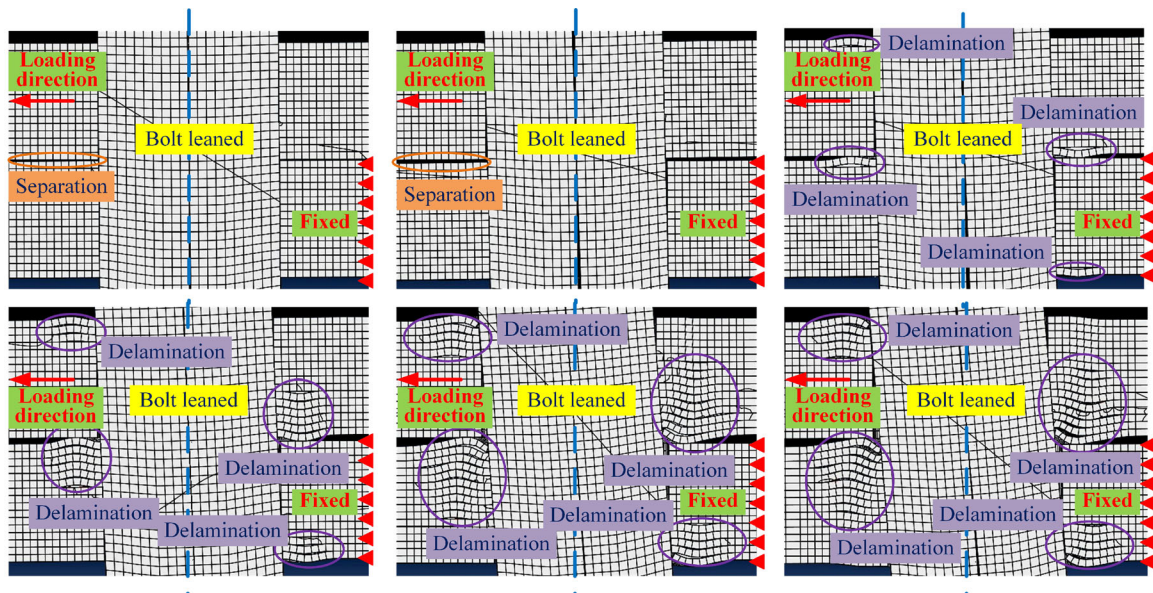


Fig. 10 Different loading stages of middle section of delamination around the hole.

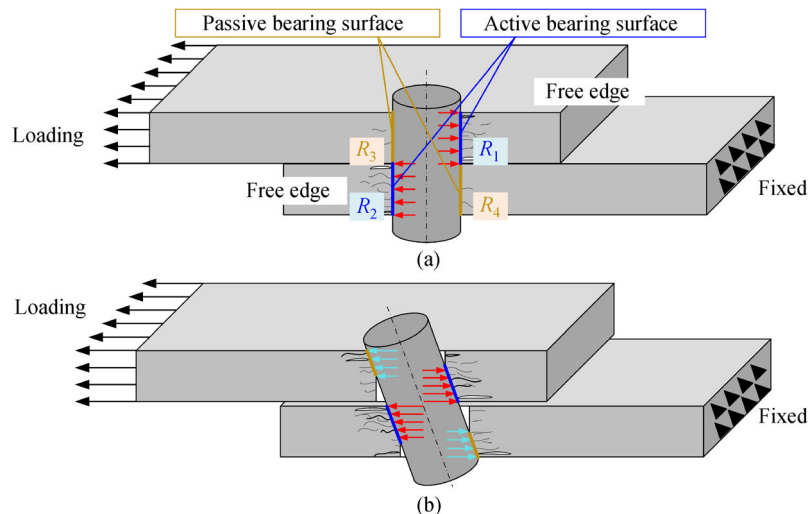


Fig. 11 Effect of secondary bending moment on load bearing mechanism: (a) Initial loading and (b) loading process.

existed, the expansion and tensile stress in the thickness direction were limited. Interaction occurred between the bolt and plate, and tangential stress concentration was observed between layers because the region was subjected to extrusion load. This result means that for unconstrained cases, delamination begins with the combined effect of normal and tangential stresses, leading to mixed modes I and II delamination. Delamination is mainly dominated by shear stress for lateral restraint cases. If the lateral restraint is strong enough to keep the interface in contact all the time, delamination will only expand in modes II and III. Thus, delamination initiation will be greatly delayed compared with the situation without a restraint. Although delamination will still occur on the upper and lower surfaces, potential delamination will expand along the thickness direction before delamination as a result of a relatively uniform stress distribution. The region will bear load together, thus effectively delaying the occurrence of delamination.

4.5 Load–displacement curve

A typical load–displacement curve of the interference-fit single lap structure is shown in Fig. 12(a). Figure 12 shows that the first half of the curve (Stage 1) is in a linear growth stage. As the load increased, the local area began to exhibit damage, and stiffness gradually decreased. With the expansion of the damage area, the ultimate bearing capacity of the overall structure was affected until the bearing strength was reached.

Figure 12(b) shows a typical load–displacement curve of the gap connection [15]. An obvious difference in the damage process was observed from the curve. The gap curve reveals three stages. Stage 1 refers to overcoming the load generated by static friction between the contact surfaces of two composite plates. Stage 2 refers to the

relative sliding between interfaces, and the bolt–hole gap gradually shrinks, leading to the final contact. In Stage 3, close contact is gradually established between the bolt and hole. The bolt begins to transfer load and the joint stiffness increases, resulting in a new linear stage. At this stage, the joint stiffness is affected by the secondary moment effect and continues to reach the joint bearing strength [15]. For interference fit, the first two stages do not exist. The load increases directly from Stage 3. Close contact is established between the bolt and hole at the beginning. During load transfer, the stress concentration is delayed, and the contact friction between the two composite plates bears a certain load.

The load–displacement curves under different interference values are shown in Fig. 13. The interference percentage corresponding to the highest strength was 0.4%, followed by 0.8%. The bearing strengths of 0% and 1.2% were almost the same, but 0% reached the bearing limit first. These results show that appropriate interference can effectively improve the bearing strength and delay the time to reach the strength limit. However, for the case without a lateral preload constraint, the value of the good interference range (0.4%–0.8%) was relatively small, which could cause difficulties during drilling and installation. This problem needs to be solved.

5 Conclusions

A static tensile test and finite element study were conducted on the bolt interference joint of a CFRP single-lap structure. The damage propagation mechanism under the influence of the secondary bending moment was analyzed, and the bearing strength under different interference percentages was predicted. The main conclusions are as follows:

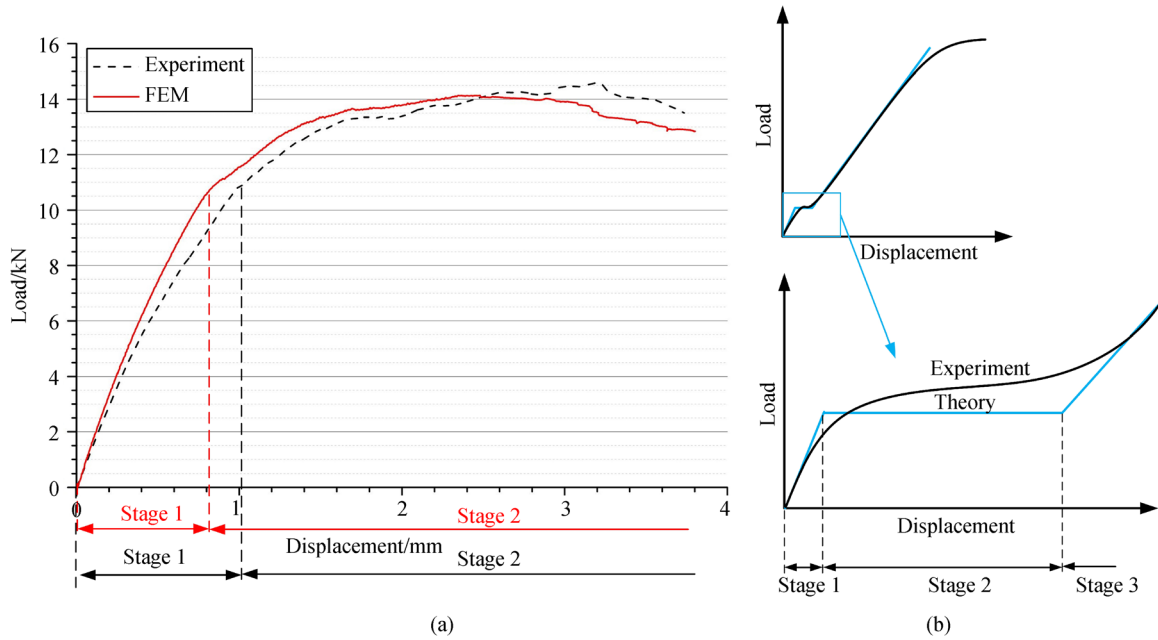


Fig. 12 Typical load–displacement curves of interference-fit structure and gap connection structure: Curves for (a) interference-fit structure and (b) gap connection structure.

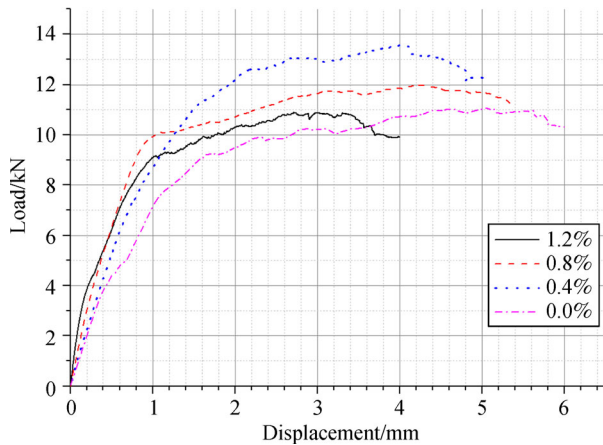


Fig. 13 Load–displacement curves for different interference percentages.

1) For a single-lap structure, the secondary bending moment and bolt rotation characteristics were evident, resulting in structural deformation, stress, and damage non-uniformity. A certain preload greatly reduced the occurrence of delamination damage.

2) For intralaminar damage, the main damage types were in-plane and out-of-plane matrix compression failure, fiber–matrix shear failure, and delamination. The damage distribution was obviously uneven along the hole thickness direction because of the secondary bending moment effect.

3) The load–displacement curve of the single-lap structure changed relatively smoothly. The first two stages

of the load displacement curve of the gap connection structure did not exist. For the studied materials and structures, the ultimate bearing strength was the highest when the interference was 0.4%.

Acknowledgements The authors declare no potential conflicts of interest with respect to the research, authorship, and/or publication of this article. This work was supported by the Aviation Science Foundation of China (Grant No. 2018ZE23011) and the National Natural Science Foundation of China (Grant No. 51275410). The authors are thankful for the support.

References

1. Cao Z Q, Cardew-Hall M. Interference-fit riveting technique in fiber composite laminates. *Aerospace Science and Technology*, 2006, 10(4): 327–330
2. Li J, Li Y, Zhang K, et al. Interface damage behaviour during interference-fit bolt installation process for CFRP/Ti alloy joining structure. *Fatigue & Fracture of Engineering Materials & Structures*, 2015, 38(11): 1359–1371
3. Zou P, Li Y, Zhang K, et al. Mode I delamination mechanism analysis on CFRP interference-fit during the installation process. *Materials & Design*, 2017, 116: 268–277
4. Zou P, Li Y, Zhang K, et al. Influence of interference-fit percentage on stress and damage mechanism in hi-lock pin installation process of CFRP. *Journal of Composite Materials*, 2017, 51(25): 3525–3538
5. Liu F L, Liu D, Liu J G. The controlling and application technology of composite structure interference installation. *Aviation Precision Manufacturing Technology*, 2011, 47(6): 36–38 (in Chinese)
6. Liu L Q, Zhang J Q, Chen K K, et al. Combined and interactive

- effects of interference fit and preloads on composite joints. *Chinese Journal of Aeronautics*, 2014, 27(3): 716–729
7. Zou P, Zhang K, Li Y, et al. Bearing strength and failure analysis on the interference-fit double shear-lap pin-loaded composite. *International Journal of Damage Mechanics*, 2016, 27(2): 179–200
 8. Kim S Y, Hennigan D J, Kim D, et al. Fatigue enhancement by interference-fit in a pin-loaded glass fibre-reinforced plastics laminate. *Proceedings of the Institution of Mechanical Engineers, Part C: Journal of Mechanical Engineering Science*, 2012, 226(6): 1437–1446
 9. Wei J C, Jiao G Q, Jia P R, et al. The effect of interference fit size on the fatigue life of bolted joints in composite laminates. *Composites. Part B, Engineering*, 2013, 53: 62–68
 10. Isbilir O, Ghassemieh E. Finite element analysis of drilling of carbon fibre reinforced composites. *Applied Composite Materials*, 2012, 19(3–4): 637–656
 11. Jiang H, Ren Y, Jin Q, et al. Flexural performances of fiber face-sheets/corrugated core sandwich composite structures reinforced by horizontal stiffeners. *International Journal of Mechanical Sciences*, 2020, 168: 105307
 12. Jiang H, Ren Y, Liu Z, et al. Evaluations of failure initiation criteria for predicting damages of composite structures under crushing loading. *Journal of Reinforced Plastics and Composites*, 2018, 37(21): 1279–1303
 13. Ren Y, Jiang H, Gao B, et al. A progressive intraply material deterioration and delamination based failure model for the crashworthiness of fabric composite corrugated beam: Parameter sensitivity analysis. *Composites. Part B, Engineering*, 2018, 135: 49–71
 14. Camanho P P, Matthews F L. A progressive damage model for mechanically fastened joints in composite laminates. *Journal of Composite Materials*, 1999, 33(24): 2248–2280
 15. Olmedo A, Santiuste C, Barbero E. An analytical model for the secondary bending prediction in single-lap composite bolted-joints. *Composite Structures*, 2014, 111(1): 354–361
 16. Xiao Y, Ishikawa T. Bearing strength and failure behavior of bolted composite joints (part I: Experimental investigation). *Composites Science and Technology*, 2005, 65(7–8): 1022–1031
 17. Zhao L, Gong Y, Zhang J, et al. Simulation of delamination growth in multidirectional laminates under mode I and mixed mode I/II loadings using cohesive elements. *Composite Structures*, 2014, 116: 509–522
 18. Chen J F, Morozov E V, Shankar K. Simulating progressive failure of composite laminates including in-ply and delamination damage effects. *Composites. Part A, Applied Science and Manufacturing*, 2014, 61: 185–200
 19. Camanho P P, Davila C G, de Moura M F. Numerical simulation of mixed-mode progressive delamination in composite materials. *Journal of Composite Materials*, 2003, 37(16): 1415–1438
 20. Riccio A, Caputo F, Di Felice G, et al. A joint numerical-experimental study on impact induced intra-laminar and inter-laminar damage in laminated composites. *Applied Composite Materials*, 2016, 23: 219–237
 21. Durão L M P, de Moura M F S F, Marques A T. Numerical simulation of the drilling process on carbon/epoxy composite laminates. *Composites. Part A, Applied Science and Manufacturing*, 2006, 37(9): 1325–1333
 22. Durão L M P, de Moura M F S F, Marques A T. Numerical prediction of delamination onset in carbon/epoxy composites drilling. *Engineering Fracture Mechanics*, 2008, 75(9): 2767–2778
 23. Feito N, Lopez-Puente J, Santiuste C, et al. Numerical prediction of delamination in CFRP drilling. *Composite Structures*, 2014, 108: 677–683
 24. Camanho P M P R de C. Application of numerical methods to the strength prediction of mechanically fastened joints in composite laminates. Dissertation for the Doctoral Degree. London: Imperial College London (University of London), 1999
 25. Xiao Y, Ishikawa T. Bearing strength and failure behavior of bolted composite joints (part II: Modeling and simulation). *Composites Science and Technology*, 2005, 65(7–8): 1032–1043